Materials Horizons

ROYAL SOCIETY OF CHEMISTRY

COMMUNICATION

View Article Online
View Journal | View Issue

Check for updates

Cite this: *Mater. Horiz.*, 2025, **12**, 2604

Received 19th November 2024, Accepted 6th January 2025

DOI: 10.1039/d4mh01665c

rsc.li/materials-horizons

Environmentally tolerant multifunctional eutectogel for highly sensitive wearable sensors†

Zhengen Wei,‡[ab] Lianghao Jia,‡[ab] Jinyu Yu,[ab] Hanrui Xu,[ab] Xing Guo,[ab] Tao Xiang *[ab] and Shaobing Zhou[ab]

Flexible hydrogel sensors have found extensive applications. However, the insufficient sensing sensitivity and the propensity to freeze at low temperatures restrict their use, particularly in frigid conditions. Herein, a multifunctional eutectogel with high transparency, anti-freezing, anti-swelling, adhesive, and self-healing properties is prepared by a one-step photopolymerization of acrylic acid and lauryl methacrylate in a binary solvent comprising water and deep eutectic solvent (DES). The results from the molecular dynamics simulations and density functional theory indicate that the hydrogen bonds between DES and water mixtures possess better stability than those between water molecules. On the other hand, DES breaks down hydrogen bonds in water, providing eutectogels with excellent anti-freezing even at −60 °C. Cetyltrimethylammonium bromide is incorporated to establish stable hydrophobic interactions and electrostatic attractions with polymer chains in the eutectogel network, resulting in superior mechanical (elongation at break of 2890%) and anti-swelling (only 2% swelling in water over 7 days) properties. The eutectogel-based strain sensors exhibit remarkable sensitivity, achieving a gauge factor of up to 15.4. The multifunctional eutectogel sensors can monitor motion and transmit encrypted information at low temperatures, demonstrating considerable potential for applications in flexible electronics within low-temperature environments.

New concepts

Flexible hydrogel sensors, recognized for their excellent flexibility, biocompatibility, and processing simplicity, have been extensively utilized in various applications, including motion monitoring, electronic skin, and human–computer interface. However, the low sensitivity restricts the application. In this study, a multifunctional eutectogel, crosslinked and stabilized by the hydrophobic interactions and electrostatic attractions, was prepared by one-step photopolymerization of acrylic acid and lauryl methacrylate in a binary solvent of water and a deep eutectic solvent. The eutectogel exhibited high transparency, anti-freezing (freezing temperatures lower than −60 °C), anti-swelling (less than 2% swelling in water over 7 days), adhesion, and self-healing properties. The strain sensors assembled based on the eutectogel showed high sensitivity with maximum gauge factor of 15.4, which was higher than other reported eutectogel sensors. The gauge factor could be adjusted by varying the binary solvent content, affecting the viscosity and ionic conductivity of solvent. The strain sensors can monitor motion and transmit encrypted information at low temperatures, demonstrating considerable potential for applications in flexible electronics within low-temperature environments.

Introduction

Flexible hydrogel sensors, recognized for their excellent flexibility, biocompatibility, and processing simplicity, have been extensively utilized in various applications, including motion monitoring, electronic skin, and human–computer interface.[1–4] However, in specific high-altitude and high-latitude regions marked by extreme climatic conditions (low temperature and aridity), hydrogels are susceptible to freezing and water loss due to their high water content. This leads to the deterioration of the fundamental properties of the hydrogel, such as flexibility and electrical conductivity, hence impacting their sensing performance.[5] Consequently, it is essential to develop materials with greater environmental tolerance to guarantee the reliable functioning of flexible sensors in extreme climatic environments.

The primary factor contributing to the freezing of hydrogels is the conversion of internal free water molecules from a disordered state to an ordered state driven by hydrogen bonding, which results in the formation of ice crystals.[6] In dry environments, the desiccation of hydrogel occurs due to the evaporation of unbound water from the hydrogel matrix into the atmosphere.[7] Consequently, it is theoretically possible to

---

[a] *Institute of Biomedical Engineering, College of Medicine, Southwest Jiaotong University, Chengdu 610031, China. E-mail: xita198906@163.com, xita198906@swjtu.edu.cn*

[b] *School of Materials Science and Engineering, Southwest Jiaotong University, Chengdu 610031, China*

† Electronic supplementary information (ESI) available. See DOI: **https://doi.org/10.1039/d4mh01665c**

‡ These authors contributed equally to this work.

achieve anti-freezing capacity and water retention simultaneously by regulating the state of water within hydrogels. Researchers have sought to fabricate environmentally adaptive hydrogels by minimizing the quantity of free water or encapsulating it within the hydrogel network using the following strategies: (1) incorporating organic solvents like glycerol, ethylene glycol, and dimethyl sulfoxide to break hydrogen bonds among the water molecules.[8–10] (2) Incorporating inorganic salts such as lithium chloride or sodium chloride to impede the formation of hydrogen bonds between water molecules through the strong hydration effects of the salts.[11–13] (3) Utilizing ionic liquids (ILs) in place of water to prepare ionic gels. ILs are organic salts with low melting points, which effectively circumvent the freeze and dehydration issues that commonly arise in hydrogels.[14,15] Nevertheless, the incorporation of inorganic salts for the synthesis of hydrogels encounters the challenge of salt precipitation, whereas the utilization of organic solvents and ILs for hydrogel fabrication gives rise to concerns about toxicity, conductivity, and cost.

Deep eutectic solvents (DESs) represent an innovative category of solvents that are environmentally benign, straightforward to prepare, cost-effective, and possess exceptional characteristics, including low melting point and low volatility.[16] Several anti-freezing and anti-drying hydrogels based on DES, called eutectogels, have been developed for use in wearable strain sensor applications.[17–19] Nonetheless, eutectogel strain sensors still present certain challenges, such as low sensitivity. This may be attributed to the high viscosity of pure DES, which impedes ionic conduction within the eutectogel, resulting in the low gauge factor (GF) of the strain sensor.[20] It has been reported that a small amount of water retention in eutectogel can reduce the viscosity of the DES and improve ionic conduction, thereby facilitating the production of high-sensitivity strain sensors. In addition, the small amount of water will not affect the anti-freezing and anti-drying properties of the eutectogel.[21] To our knowledge, there is limited research investigating the impact of water and DES content on sensitivity in eutectogel-based wearable strain sensors. Therefore, we believe that elucidating the interaction between DES and water in eutectogel and investigating the effects of DES and water content on the sensitivity of strain sensors are crucial for the advancement of environmentally tolerant multifunctional eutectogel strain sensors.

In this study, we developed environmentally tolerant eutectogels with high transparency, anti-freezing, anti-swelling, adhesive, and self-healing properties for highly sensitive flexible wearable strain sensors (Fig. 1(a)–(c)). The eutectogels were prepared by a one-step photopolymerization of acrylic acid (AA) and lauryl methacrylate (LMA) in a binary solvent consisting of water and DES based on choline chloride (ChCl) and ethylene glycol (EG), named PAL. Surfactant cetylammonium bromide (CTAB) was added to form stable hydrophobic associations and electrostatic attraction in the eutectogel network. The excellent environmental tolerance of PAL eutectogels (freezing temperature < -60 °C) mainly originates from the hydrogen bonding between DES and water molecules, which has been investigated from molecular/atomic and energy levels by molecular dynamics (MD) simulations and density functional theory (DFT). Hydrophobic association and electrostatic attraction constitute dynamic physical cross-linking points, which endow the eutectogels with good mechanical stability, anti-swelling, and self-healing properties. The abundance of –COOH and $-COO^-$ groups in the eutectogels makes them highly adhesive to different substrate materials. Furthermore, we assembled the PAL eutectogel into a strain sensor, which demonstrated high sensitivity (with a GF of up to 15.4) and good stability (8000 cycles). The effects of DES and water content on the sensitivity were investigated. Finally, we employed the strain sensor for motion monitoring and encrypted message transmission at -30 °C, and the findings indicate that the sensor can produce steady and distinct signals. Overall, a multifunctional eutectogel with environmental tolerance has been developed, demonstrating considerable potential for application in flexible sensors under low-temperature conditions.

Results and discussion

Fabrication of eutectogels

The synthesis of DES based on EG and ChCl in a molar ratio of 2 : 1 was referenced from previous work (Fig. S1, ESI†).[22] EG and ChCl are bonded together by hydrogen bonding, which significantly reduces the melting point of the composite (Fig. S2, ESI†). The binary solvent, comprising DES and water as the dispersion medium for PAL eutectogels, has been demonstrated to effectively prevent the eutectogels from freezing at low temperatures. This phenomenon can be attributed to the ability of DES to disrupt the ordered arrangement of water molecules. Consequently, the water molecules in the binary solvent are rendered in a disordered state without freezing (Fig. 1(d)). PAL eutectogels were prepared *via* free radical copolymerization of AA and LMA in the binary DES/H_2O solvents with the presence of CTAB. The DES contents were 0, 33, 50, 66, and 100 wt% of the total solvent mass, with the corresponding PAL eutectogels designated as PAL0, PAL33, PAL50, PAL66, and PAL100, respectively. The molecular chain P (AA-*co*-LMA) inside the eutectogel is a copolymer composed of hydrophilic AA and hydrophobic LMA. The hydrophobic interactions between LMA and CTAB can serve as physical cross-linking points, allowing P(AA-*co*-LMA) to maintain a stable three-dimensional network structure in DES/H_2O binary solvents. The hydrophobic association of the LMA units and the hydrogen bonding between the AA units endow the eutectogel with good self-healing capability. Furthermore, the –COOH groups and ionized $-COO^-$ groups on the P(AA-*co*-LMA) polymer chains can form hydrogen bonds and electrostatic attractions with diverse surfaces, thereby conferring the eutectogel with good adhesion properties. The successfully prepared eutectogels with different proportions of DES/H_2O were transparent. The transparency of PAL66 eutectogel was measured using a UV-Vis spectrophotometer in the range of 400 nm to 800 nm, which showed that the transmittance of PAL66

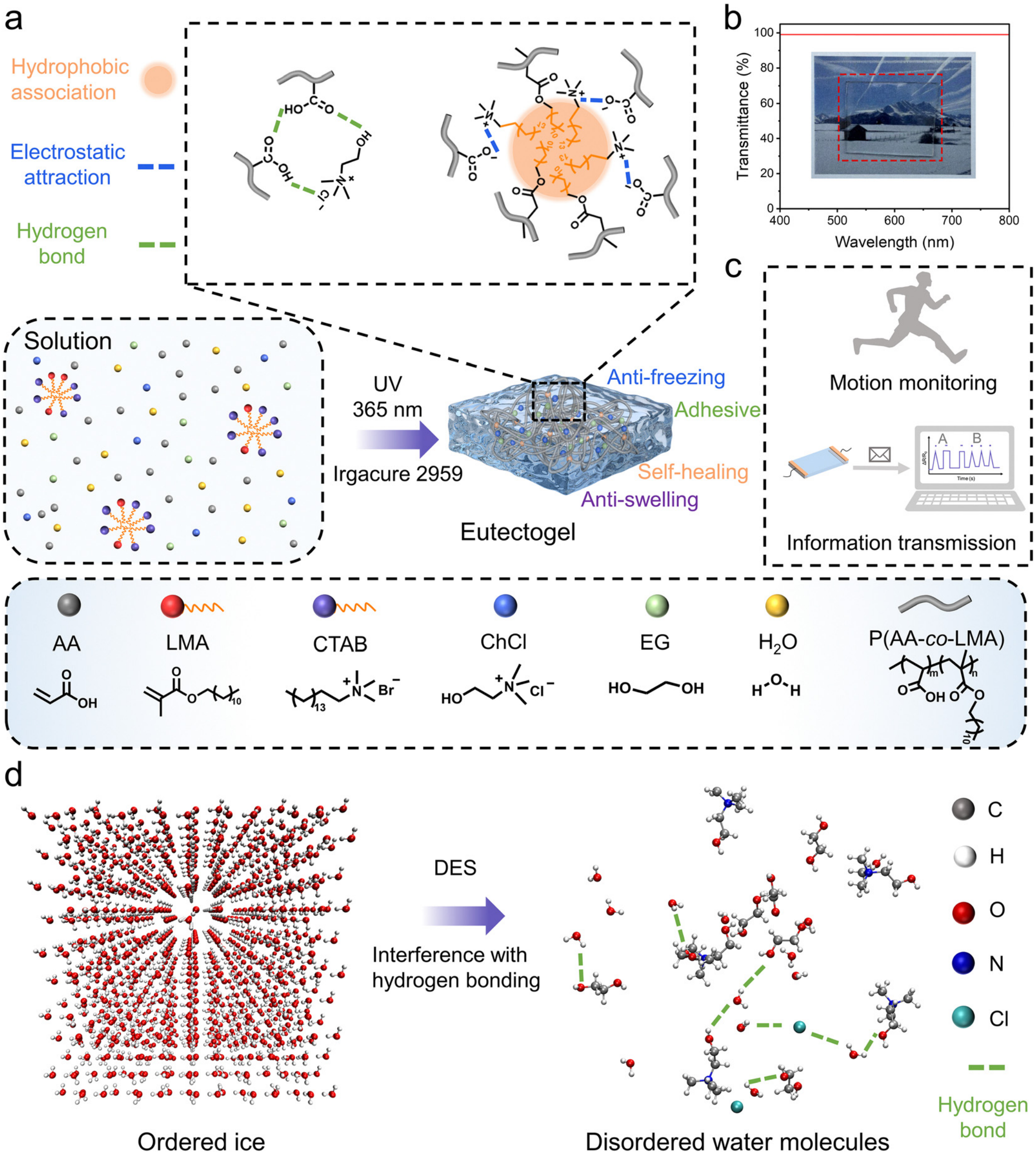

Fig. 1 Fabrication, chemical structure, and performance of PAL eutectogel. (a) Schematic illustration of the fabrication, interactions, and properties of the eutectogel. (b) Transparency of the eutectogel. (c) Applications of eutectogel for motion monitoring and information transmission. (d) Hydrogen bonding interactions between DES and water molecules.

eutectogel was 99% (Fig. 1(b)). The degree of reactivity of free radical polymerization was investigated using attenuated total reflection-Fourier transform infrared spectroscopy (ATR-FTIR). The FTIR spectra of the precursor solution and the PAL66 eutectogel demonstrated that the characteristic peak at $\sim$1635 cm^{-1}, attributed to vinyl, disappeared (Fig. S3, ESI†), indicating that the monomers were fully polymerized.

Mechanical properties

Good mechanical properties in sensors ensure stable output signals. The influence of DES content in the solvent on the mechanical properties of PAL eutectogels was examined (Fig. 2(a)). As shown in Fig. 2(b), the elongation at break significantly increased with increasing DES content, from 1086% to 3107%. However, the Young's modulus and tensile strength decreased obviously (Fig. 2(c)). In particular, when the DES content increased from 66 wt% to 100 wt%, Young's modulus and tensile strength significantly decreased by 76.30% and 92.78%, respectively. This is attributed to the disruption of the hydrophobic associations that serve as physical cross-linking points in the PAL eutectogels. Hydrophobic association in PAL eutectogel systems is driven by the hydrophobic LMA units on the P(AA-*co*-LMA) chains and the hydrophobic ends of the surfactant CTAB, which repel water molecules in the solution, leading to the formation of hydrophobic clusters.[23] As the DES content increased, the solution environment transitioned from pure water to a binary solvent, and then to pure DES. This transition disrupted the

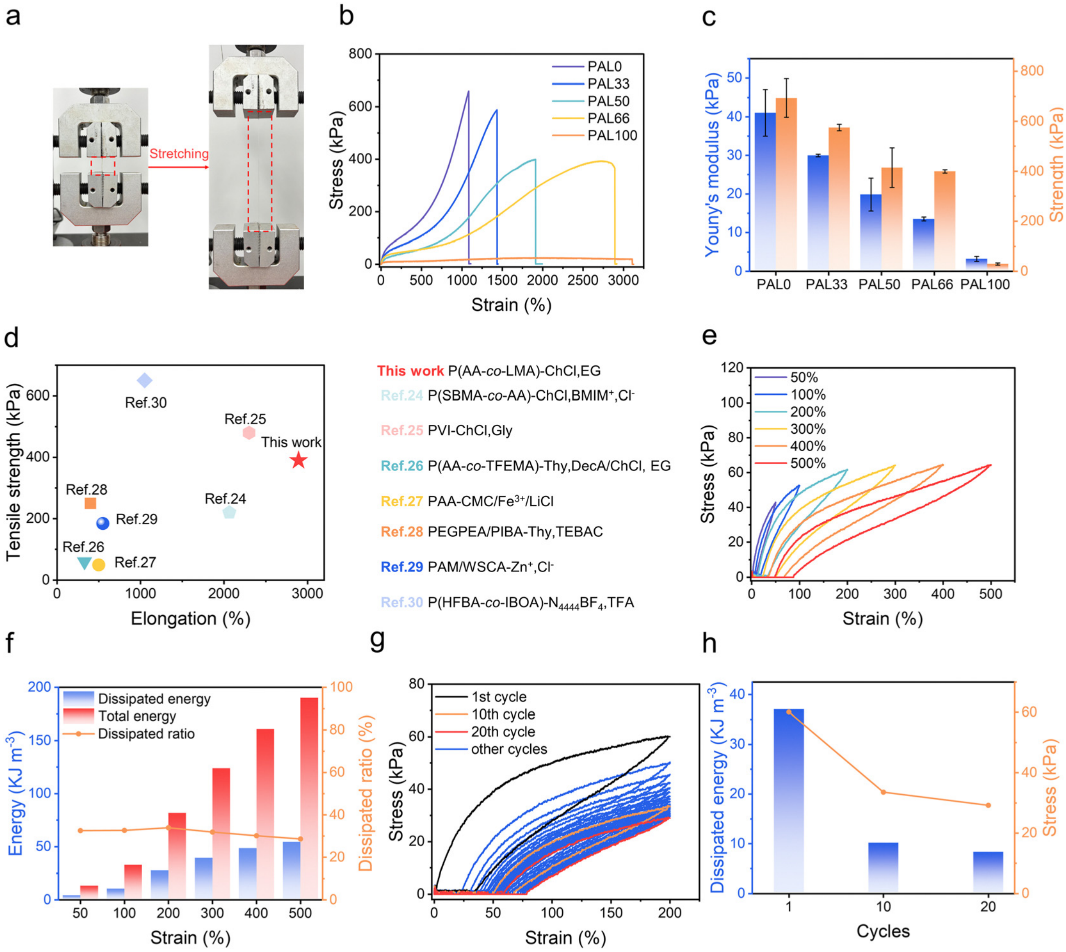

Fig. 2 Mechanical properties of PAL eutectogels. (a) Photographs of PAL eutectogels tensile test. (b) Tensile stress–strain curves of PAL eutectogels. (c) Young's modulus and tensile strength of the PAL eutectogels. (d) Comparison of tensile strength and elongation of PAL66 with other reported eutectogels. (e) Continuous loading–unloading tensile tests of PAL66 eutectogel at different strains from 50% to 500%. (f) The calculated total energy, dissipated energy, and dissipated ratio of PAL66 eutectogel. (g) Performance of PAL66 eutectogel in 200% strain 20 cycles loading–unloading tensile test. (h) The corresponding maximum tensile stress and dissipated energy per cycle.

hydrophobic associations, leading to a reduction in crosslink density and a consequent decrease in the Young's modulus and tensile strength. When the DES content reached 100 wt%, the eutectogel's Young's modulus and tensile strength became too low. In addition, the PAL66 eutectogel demonstrated favorable mechanical stability and stretchability compared to similar gels based on pure DES or DES/H_2O binary solvents as dispersion medium (Fig. 2(d)).[24–30] Therefore, considering tensile properties, modulus, and strength, the PAL66 eutectogel was selected for further testing. The cyclic tensile performance of PAL66 eutectogel during continuous loading and unloading (strain increased from 50% to 500%) was evaluated (Fig. 2(e)). The corresponding energy dissipation per cycle was calculated, showing an increase from 4.35 kJ m^{-3} to 54.41 kJ m^{-3} (Fig. 2(f)). The energy dissipation rate reached more than 28% per cycle. Furthermore, cyclic tensile tests were performed on PAL66 eutectogel at a fixed strain of 200% (Fig. 2(g)), and energy dissipation was calculated (Fig. 2(h)). The energy dissipation of 37.05 kJ m^{-3} for the first cycle was 3.6 times and 4.4 times higher than that of the tenth (10.18 kJ m^{-3}) and twentieth cycles (8.35 kJ m^{-3}), respectively. The maximum stress in the twentieth cycle (29.18 kPa) was approximately 49% of that in the first cycle (60.08 kPa). This suggests that the maximum energy dissipation occurs during the first cycle in the cyclic tensile test, which correlates with the phenomenon of weaker non-covalent interactions being broken. A significant residual strain was observed after 20 cycles of loading–unloading, which returned the PAL66 eutectogel to its original state after being left to stand for 0.5 h (Fig. S4, ESI†). In order to ascertain the recoverability of PAL66 eutectogel following 20 cycles of stretching, the material was subjected to uniaxial stretching, resulting in the generation of a stress–strain curve (Fig. S5, ESI†). The findings indicate that the stress can be recovered to 81% of the original state, while the strain can be recovered to 97% of the original state. This behavior is attributed to the destruction of some physical cross-links of the PAL66 eutectogel during the continuous deformation process. The ability of the eutectogel to return to its original state is due to the reconstruction of these physical cross-links. This mechanism of destruction and reconstruction effectively prevents material failure caused by stress concentration during repetitive deformation. Subsequently, the compression properties of PAL66 eutectogels were characterized (Fig. S6, ESI†), and the PAL66 eutectogels showed residual strain and energy dissipation behaviors during compression, attributed to the disruption and remodeling mechanisms of the physical cross-linking points.

Environment tolerance performance

The environmental tolerance of eutectogels is crucial for the functionality of wearable sensors. Eutectogel strain sensors frequently encounter complex environments in practical applications, such as low temperatures, aridity, exposure to acidic and alkaline solutions, *etc.* We first investigated the capacity of PAL eutectogels to adapt to dry environments (25 °C and 30% relative humidity). As shown in Fig. S7 (ESI†), the PAL66 eutectogel retained 86% of its initial mass after 24 h, while the mass of the DES-free PAL0 hydrogel was only 51% of its initial value. The excellent environmental adaptability ability of the PAL66 eutectogel is attributed to the low volatility of DES and its ability to interact with water molecules. Then we investigated the swelling resistance of PAL66 eutectogel, and the results are shown in Fig. S8 (ESI†). PAL66 eutectogel demonstrated effective swelling resistance in both neutral (pH = 7) and weak acid (pH = 5) solutions, exhibiting a swelling rate of less than 2% for the 7-day immersion period. Additionally, in a strongly acidic solution (pH = 3), it retained a certain degree of swelling resistance, with a swelling rate of 73%. The establishment of a stable hydrophobic association zone between the P(AA-*co*-LMA) molecular chain and CTAB accounts for this result. In alkaline solutions with pH values of 9 and 11, PAL eutectogels exhibit a loss of anti-swelling properties. This phenomenon is attributed to two distinct but interrelated mechanisms. The alkaline environment facilitates the ionization of –COOH, thereby enhancing the hydrophilic character of the molecular chains. Furthermore, it interferes with the hydrophobic binding zones established by the combined effects of hydrophobic interactions and electrostatic attraction.[31–33] This facilitates the penetration of water molecules into the eutectogel.

The PAL eutectogels were subjected to a −60 °C environment to investigate their anti-freezing performance, as shown in Fig. S9 (ESI†). Following 2 h in the cold trap at −60 °C, the PAL0, PAL33, and PAL50 samples exhibited freezing and a color change from their original transparent state to white. In contrast, the PAL66 and PAL100 samples with high DES content remained transparent. The PAL0 and PAL66 samples were observed separately (Fig. 3(a)). The PAL66 eutectogel demonstrated the capacity to remain unfrozen at −60 °C while maintaining flexibility, whereas the PAL0 eutectogel underwent freezing. The mechanical properties of PAL eutectogels were examined at different temperatures using dynamic mechanical analysis (DMA). From the tensile stress–strain curves at different temperatures, it can be seen that the Young's modulus of the PAL eutectogels increases with decreasing temperature (Fig. 3(b)). At −60 °C, the PAL0 hydrogel undergoes complete freezing, resulting in the loss of tensile properties and a significant increase in modulus, with stress levels reaching 2.93 MPa at 6% strain. The PAL66 eutectogel remained unfrozen at temperatures as low as −60 °C, with an insignificant increase in modulus, and still exhibited good tensile properties. To further investigate the effect of temperature on the mechanical properties of PAL eutectogels, temperature scans were conducted using DMA to evaluate their storage modulus (G') and loss modulus (G''). The results of these scans are presented in Fig. S10 (ESI†). A decline in temperature to −4 °C results in a marked increase in the G' and G'' of PAL0 eutectogel, accompanied by a discernible peak in the loss angle tangent ($\tan\delta$) curve. In contrast, although G' and G'' of PAL66 eutectogel also increase during the temperature decrease, there is no obvious abrupt change, and the $\tan\delta$ curve is relatively flat. This suggests that PAL66 eutectogel does not freeze within the scanning temperature range. The anti-freezing performance of the PAL eutectogel was analyzed by differential scanning calorimetry (DSC), and the resulting cooling–heating process curve from 25 °C to −80 °C is presented in Fig. 3(c). During the cooling and heating process, the PAL0 hydrogel exhibited distinct exothermic and heat absorption peaks at −21 °C and 0 °C, respectively. These peaks were attributed to the freezing and melting of water within the PAL0 hydrogel. In contrast, the cooling–heating process curve of PAL66 eutectogel did not exhibit any exothermic or heat absorption peaks. This suggests that PAL66 did not undergo crystallization during the cooling process from 25 °C to −80 °C.

DES can establish hydrogen bonds with water molecules, thereby incorporating them into the eutectogel and inhibiting the freezing of water molecules due to the ordering induced by hydrogen bonding. To investigate the interaction between DES and water molecules in PAL eutectogel, we selected PAL66 eutectogel as a representative for molecular dynamics (MD) simulations. As illustrated in Fig. S11 (ESI†), six distinct types of hydrogen bonds are observed in the molecular dynamics snapshot. The choline cation (Ch^+) and ethylene glycol (EG) in DES can simultaneously serve as both hydrogen bond donors (HBD) and acceptors (HBA), whereas the chloride ion (Cl^-) can act exclusively as the HBA.[34] This results in the formation of 5 types of hydrogen bonds between the water molecule and DES, and a 6th type of hydrogen bond between water molecules. The distribution relationship between the HBDs and HBAs involved in hydrogen bonding interactions can be elucidated by plotting the radial distribution function (RDF) of the corresponding particles (Fig. S12, ESI†). The size of the first peak of the RDF quantifies the probability that the first nearest-neighbor particle occurs at a specific distance from the center particle. The peak indicates the probability of the particle appearing at that particular distance. The first peak of the Cl^-_{ChCl}–H_{water} RDF curve reaches 10.2, which is significantly higher than the other interacting particles. This finding suggests that the H_{water} atoms were most likely to form hydrogen bonds with Cl^-_{ChCl}. This is because all six types of hydrogen bonds previously discussed are of medium strength and are dominated by

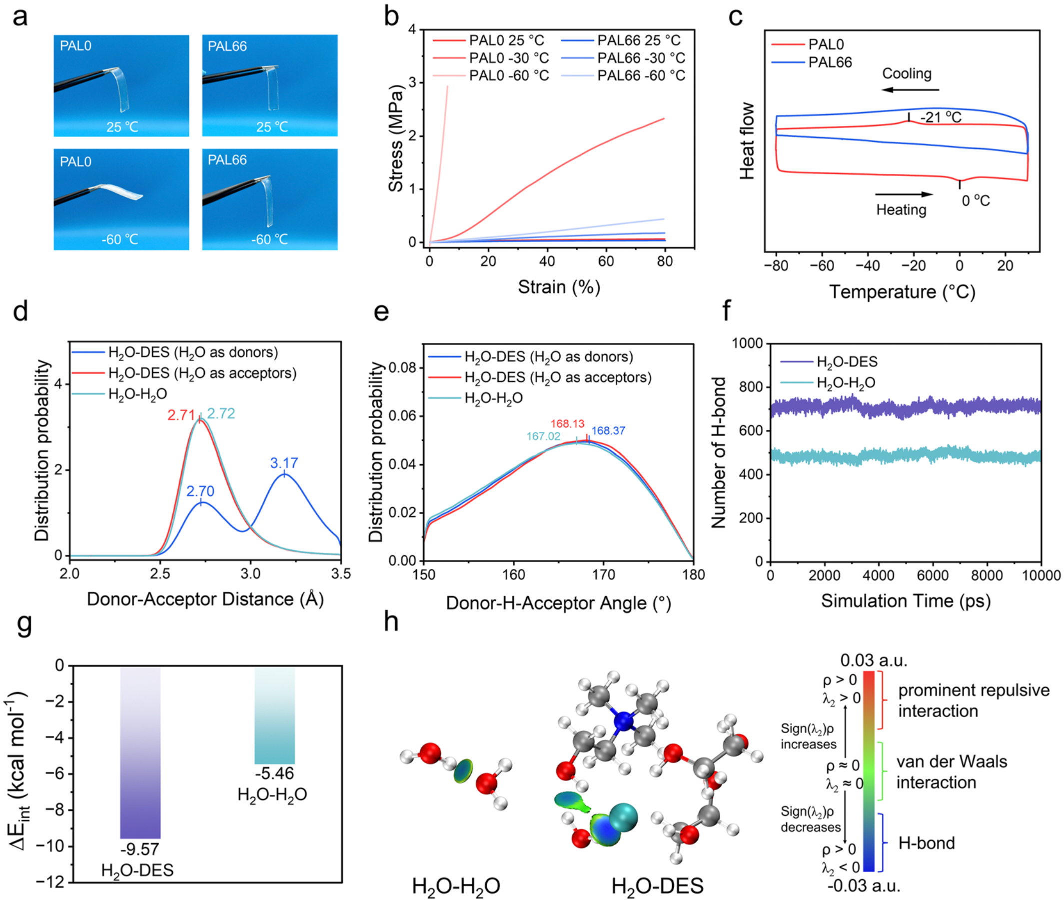

Fig. 3 Anti-freezing performance of PAL eutectogels. (a) Digital photographs of PAL0 and PAL66 eutectogels at 25 °C and −60 °C. (b) Tensile stress–strain curves of PAL0 and PAL66 at different temperatures. (c) DSC curves of PAL0 and PAL66 eutectogels. (d) Probability density function of hydrogen bond donor–acceptor distance. (e) Probability density functions for hydrogen bond donor–acceptor angle. (f) Type of hydrogen bonds and the number as functions of simulation time. (g) Binding energy of H_2O–H_2O and H_2O–DES. (h) IGMH three-dimensional diagram of H_2O–H_2O and H_2O–DES.

electrostatic attraction.[35] The electrostatic attraction between negatively charged Cl^-_{ChCl} and H_{water} is considerably stronger than that between uncharged neutral O and H_{water}, resulting in a higher probability of hydrogen bond formation between Cl^-_{ChCl} and H_{water}. Subsequently, an analysis of the geometrical characteristics and number of hydrogen bonds was conducted based on the results of molecular dynamics trajectories. The criteria for determining the formation of hydrogen bonds between particles are as follows: first, the donor–acceptor distance must be less than 3.5 Å; second, the donor-H-acceptor angle must range from 150° to 180°. The six types of hydrogen bonds in the system can be categorized into three groups: one for H_2O–DES (H_2O as donor), another for H_2O–DES (H_2O as acceptor), and a third for H_2O–H_2O. Fig. 3(d) and (e) illustrate the probability density functions (PDF) for the donor–acceptor distances and the donor-H-acceptor angles, respectively. The H_2O–DES (H_2O as donor) donor–acceptor distance PDF curves show two peaks, the peak at 3.17 Å is the distance between the O_{water} and the Cl^-_{ChCl}, and the peak at 2.70 Å corresponds to the distance between the O_{water} and the O_{ChCl}. The H_2O–DES (H_2O as acceptor) and H_2O–H_2O donor–acceptor distance PDF curves have only one peak at 2.71 Å and 2.72 Å, respectively. The PDF curves of donor-H-acceptor angles for all three types of hydrogen bonds have only one peak located at 168.37°, 168.13° and 167.02°, respectively. This result indicates that stable hydrogen bonds are formed within the PAL66 eutectogel system and the geometrical features of the hydrogen bonds are very similar. Then, we counted the number of hydrogen bonds formed between H_2O and DES and H_2O and H_2O, respectively (Fig. 3(f)). The average number of H_2O–DES hydrogen bonds reached 709 higher than that of H_2O–H_2O hydrogen bonds (485), which intuitively demonstrated from the atomic level that DES could interfere with the formation of hydrogen bonds between water molecules, thus conferring the environmental tolerance property to PAL66 eutectogel. Furthermore, the energetic aspects of hydrogen bonding between water molecules and other components of the eutectogel have been investigated by density functional theory simulation (DFT) (Fig. S13, ESI†). The binding energy of H_2O–DES was found to be -9.57 kcal mol^{-1}, higher than the binding energy of H_2O–H_2O (-5.46 kcal mol^{-1}) (Fig. 3(g)). To visualize the hydrogen bonding in the H_2O–DES system and the H_2O–H_2O system, an analysis of the hydrogen bonding interactions was conducted using the Independent Gradient Model based on the Hirshfeld

Partition (IGMH) method. The results are illustrated in Fig. 3(h), wherein the blue-green isosurfaces delineate the hydrogen bonding interactions in the H_2O–DES system and the H_2O–H_2O system. Notably, the isosurfaces of the H_2O–DES system exhibit a darker hue. This suggests that the hydrogen bond formed between H_2O and DES is more stable than that formed between water molecules. Therefore, DES can interfere with hydrogen bonding between water molecules and form more stable hydrogen bonds with water molecules, thus preventing PAL66 eutectogels from freezing at low temperatures and losing water in dry environments.

Adhesion and self-healing properties

Flexible sensors necessitate a stable connection with the substrate to ensure accurate signal collection in practical applications. The adhesion properties of the eutectogel are critically significant. The PAL66 eutectogel exhibits effective adhesion properties across various common substrates, including silicone pad, glass, plastics, copper sheets, wood, and steel (Fig. 4(a)). The P(AA-*co*-LMA) polymer chain within the PAL66 eutectogel contains a multitude of –COOH and ionized $–COO^-$ groups. Therefore, the adhesion between the eutectogel and the substrate can be attributed to hydrogen bonding interactions and electrostatic attraction.[8] The adhesion between the eutectogel and metal surfaces is primarily driven by electrostatic attraction, whereas the adhesion to surfaces of substrates such as silicone pad, glass, plastic, and wood is predominantly facilitated by the formation of hydrogen bonding interactions (Fig. 4(b)). The lap-shear tests were conducted to quantify the adhesion strength of the PAL66 eutectogel, with all eutectogel samples cut to a uniform size of $10 \times 10 \times 1\ mm^3$ (Fig. 4(c)). The results are shown in Fig. 4(d) and (e). The PAL66 eutectogel demonstrated favorable adhesion when tested with a variety of materials, including silicone pad (22.11 kPa), glass (25.53 kPa), copper (22.81 kPa), and wood (14.24 kPa). However, flexible sensors are exposed to much harsher environments in

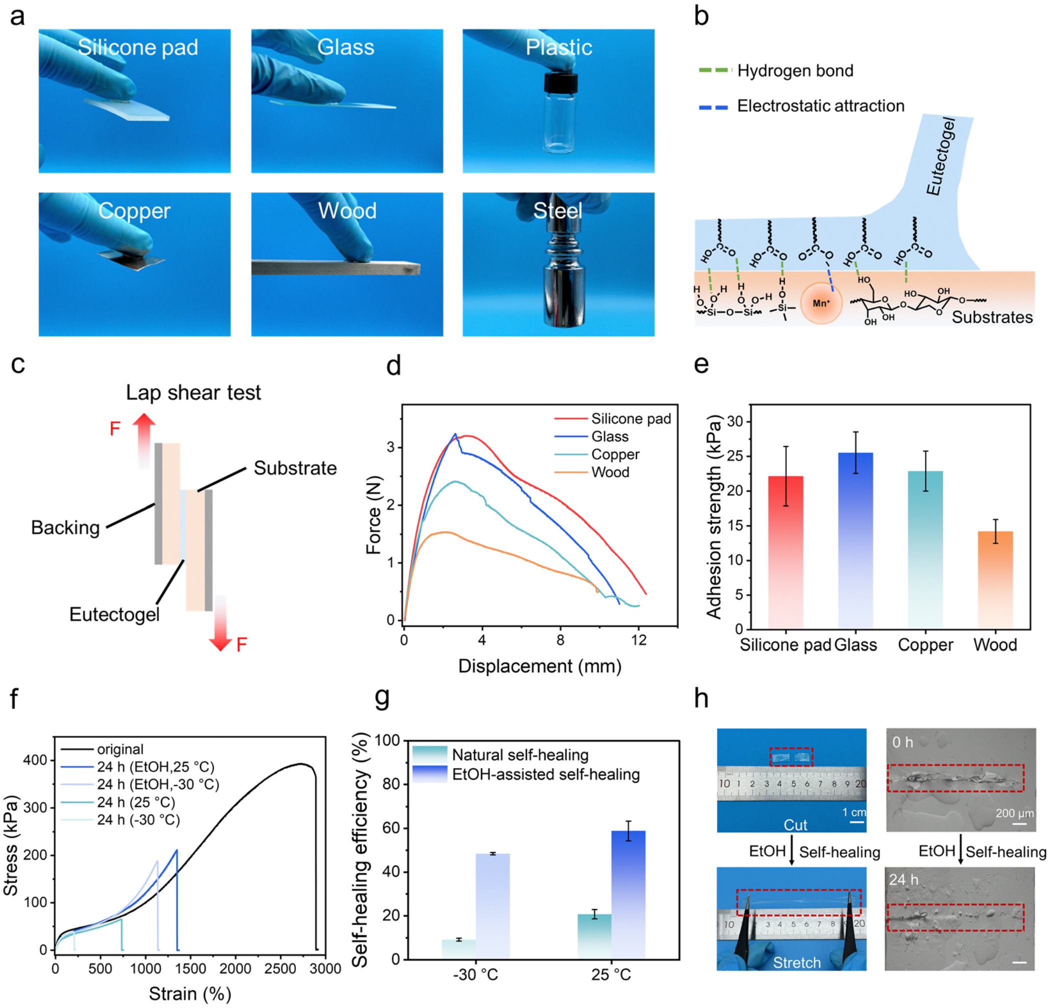

Fig. 4 Adhesion and self-healing properties of PAL66 eutectogel. (a) Digital photographs of PAL66 eutectogel adhered to various substrates. (b) Adhesion mechanisms between PAL66 eutectogels and different substrates. (c) Schematic diagram of lap shear test. (d) Adhesion force curves using different substrates. (e) Adhesion strength between PAL66 and different substrates. (f) Stress–strain curves of the original and healed PAL66 eutectogel after various healing times and temperatures. (g) Self-healing efficiency of PAL66 eutectogel at various healing times and temperatures. (h) Digital photographs of PAL66 eutectogel self-healing and optical microscope images of scratch experiments.

practical applications. The adhesion ability of PAL66 eutectogel was initially examined in a high-humidity (25 °C, 90% relative humidity) environment, and the results are presented in Fig. S14a and b (ESI†). The adhesion strengths of PAL66 eutectogel with silicone pad, glass, copper, and wood are 30.60 kPa, 22.26 kPa, 17.41 kPa, and 33.71 kPa. The adhesion strength of PAL66 eutectogel with glass and copper was observed to undergo a slight decrease, while the adhesion strength with silicone pad and wood was found to undergo an enhancement. These findings indicate that PAL66 eutectogel retains satisfactory adhesion properties in high humidity environments. Subsequently, copper, which exhibits the poorest adhesion strength in high humidity environments, was selected as a representative substrate, and the adhesion performance of PAL66 eutectogel in varying pH levels (pH = 3, 5, 7, 9, 11) was further investigated (Fig. S14c and d, ESI†). The lowest adhesion strength (~14.58 kPa) was observed at pH 7, which was lower than that of the high humidity environment. Conversely, the adhesion strength increased when the pH was either acidic or alkaline compared to that of the high humidity environment. This phenomenon could be attributed to the fact that acidic and alkaline solutions corroded the surface of the copper sheet, resulting in a roughened surface that enhanced the adhesion between PAL66 eutectogel and the copper sheet. The findings indicate that PAL66 eutectogel maintains robust adhesion on surfaces with which acidic or alkaline solutions are in contact. We also selected glass, which exhibits a reduced adhesion strength in high humidity environments, as a substrate and examined the adhesion performance of PAL66 eutectogel at varying pH levels. As illustrated in Fig. S14c and d (ESI†), the adhesion strength of PAL66 eutectogel on glass substrates at varying pH levels was determined to be 14.72 kPa, 15.82 kPa, 13.74 kPa, 17.11 kPa, and 13.55 kPa, respectively. The findings of the study demonstrated that the adhesion performance of PAL66 eutectogel remains unaltered under varying pH levels.

Besides adhesion properties, multiple non-covalent interactions confer self-healing properties to PAL eutectogels. The self-healing properties of the material can prolong its lifetime and diminish the potential for environmental contamination. A series of experiments were conducted to investigate the self-healing properties of eutectogels. The eutectogel was cut in half and subsequently assembled at 25 °C and −30 °C for a specified duration. Uniaxial tensile experiments were conducted, and the results are shown in Fig. 4(f), (g) and Table S2 (ESI†). The eutectogel exhibited self-healing efficiencies of 17.39%, 18.19%, and 20.71% at 25 °C over durations of 6 h, 12 h, and 24 h, respectively. At an ambient temperature of −30 °C, the self-healing efficiencies of the eutectogel were recorded at 8.42%, 9.12%, and 9.20%, indicating a significant inefficiency in self-healing capabilities. This is because only the hydrogen bonds and a limited number of hydrophobic association regions can be disrupted and rebuilt during the self-healing process (Fig. S15a, ESI†). It has been reported that the use of ethanol (EtOH) can disrupt hydrophobic associations, thus facilitating the diffusion of the polymer molecular chains to the interface and the formation of a variety of interactions (electrostatic attraction, van der Waals forces, and hydrophobic association reconfiguration).[33] Anhydrous EtOH was applied to the two sections of the PAL66 eutectogel that had been cut in half. After the EtOH evaporated for a while, the two halves of the eutectogel were spliced together and the eutectogel could be stretched to a certain length. The optical photos at the eutectogel section revealed that most of the gaps had been restored (Fig. 4(h)). As illustrated in Fig. S15b (ESI†), the natural self-healing process is limited to the reforming of hydrogen bonds. After EtOH treatment, both hydrophobic associations and hydrogen bonds in the eutectogel participate in the self-healing process, thereby enhancing the eutectogel's self-healing efficiency. Subsequently, the EtOH-assisted self-healing properties of PAL66 eutectogel were investigated through uniaxial tensile testing. The self-healing efficiency of PAL66 eutectogel was observed to increase with the healing time, reaching 58.82% after 24 h of healing at 25 °C. Furthermore, the self-healing performance of PAL66 eutectogel was evaluated in a temperature-controlled environment at −30 °C. The observed trends were comparable to those observed at 25 °C. The self-healing efficiency of the eutectogel was determined to be 48.42% after 24 h of healing. This is markedly higher than the self-healing efficiency of the natural self-healing process, which is approximately 2.8 times higher at 25 °C and 5.3 times higher at −30 °C. The self-healing at low temperatures is attributed to the coupling of the anti-freezing and self-healing properties of the PAL66 eutectogel. The effective anti-freezing facilitates the mobility of P(AA-*co*-LMA) molecular chains to move even at low temperatures of −30 °C, which aids in the reconfiguration of the hydrogen bonding and reformation of hydrophobic association regions.

Strain sensing performance

The PAL66 eutectogel exhibits excellent mechanical characteristics, notable flexibility, adhesion properties, self-healing capabilities, and exceptional anti-freezing properties. The assembly of resistive sensors was conducted using eutectogels, aimed at evaluating its strain sensing performance (Fig. S16, ESI†). The parameter GF, which is used to quantify the sensitivity of the strain sensors, was subjected to testing, and the results are presented in Fig. 5(a) and (Fig. S17, ESI†). The results of the study indicate that the GF of the eutectogel strain sensor exhibits an initial increase, followed by a subsequent decrease, with an increase in water content. Furthermore, the maximum GF of the eutectogel strain sensors is observed to be at its zenith when the water content reaches one-third of the binary solvent. This is because the resistance change is crucial for the GF of eutectogel, which is an ionic conductor, and the number of ions and ionic conduction rate in turn determine the resistance of eutectogel. Water can modulate the DES solvent viscosity and increase the ionic conduction rate in eutectogels, however, too high a water content will result in a decrease in the number of ions inside the eutectogel, so the proper water content allows the number of ions inside the eutectogel and the ionic conduction rate to be balanced, thus increasing the GF of the eutectogel strain sensor.[17,20,21] The

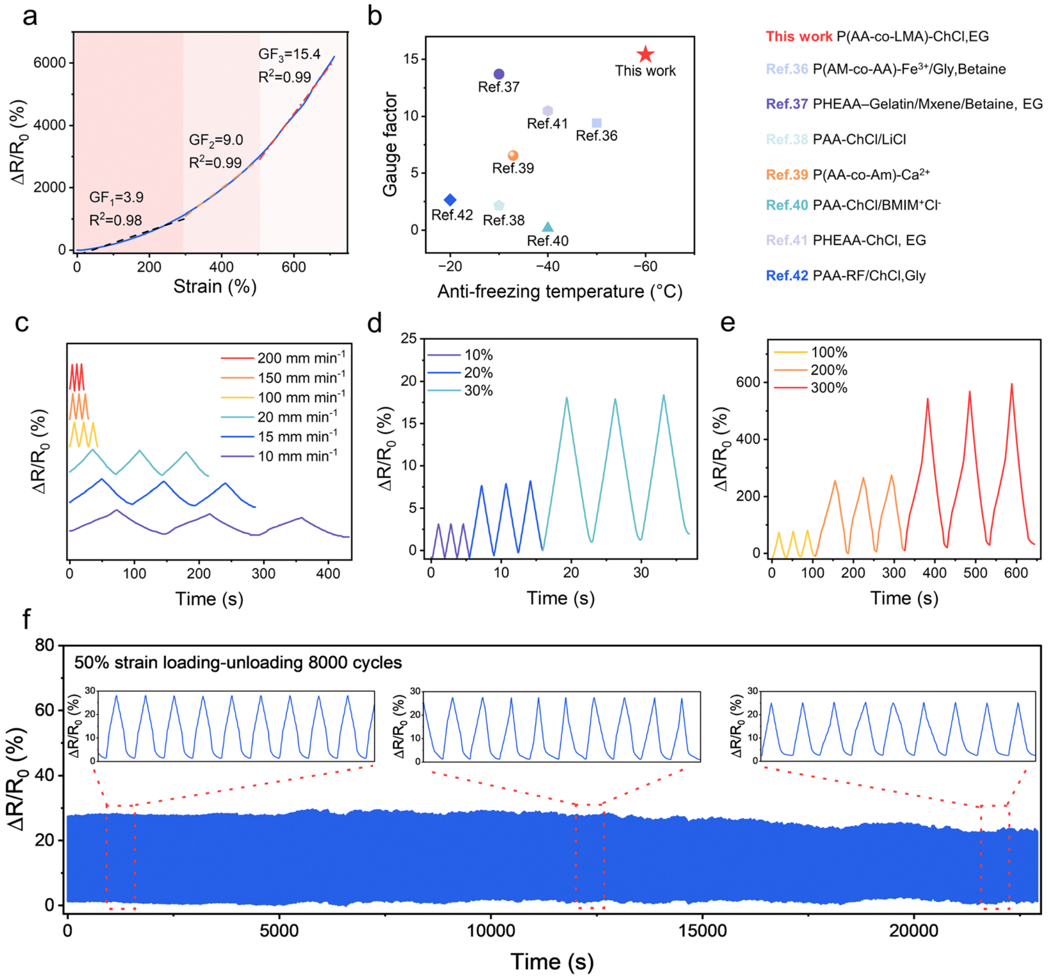

Fig. 5 Performance of strain sensors based on PAL66 eutectogel. (a) Relative resistance *versus* strain curve of PAL66 eutectogel strain sensor. (b) Comparison of the PAL66 eutectogel-based strain sensor with previously reported eutectogel-based strain sensors on two key performance parameters: GF (preferred to be higher) and anti-freezing temperature (preferred to be lower). (c) Change in relative resistance of PAL66 eutectogel strain sensor stretched to 50% at different stretching rates. (d) and (e) Relative resistance changes of PAL eutectogel strain sensor during progressive cyclic loading at small strains (10–30%) and large strains (100–300%). (f) Relative resistance variation of the PAL66 eutectogel strain sensor under cyclic loading–unloading with 50% tensile strain for 8000 cycles.

linear range of the PAL66 eutectogel can be delineated into three distinct regions: 0–300% strain, 300–500% strain, and 500–700% strain. The corresponding GF of these regions is 3.9, 9.0, and 15.4, respectively. It is notable that the GF value exhibits an increasing trend with the elevation of tensile strain. This phenomenon can be attributed to the reduction in the cross-sectional area of the PAL66 eutectogel during the stretching process, which results in a slower rate of ion transport and an increase in the relative resistance of the eutectogel. We compared the two indexes of GF and freezing temperature of PAL66 eutectogel with the anti-freezing eutectogel strain sensors that have been reported (Fig. 5(b)). The PAL66 eutectogel exhibits an operating frost resistance of −60 °C and a GF of up to 15.4, which affords it a significant advantage over other DES-based hydrogel strain sensors.[36–42] PAL eutectogels were prepared using UV photopolymerization, and to demonstrate the reproducibility of their performance, we conducted an examination of the strain sensing performance of the regions located on the four edges of the same eutectogel (Fig. S18a, ESI†). Fig. S18b–e (ESI†) illustrates the relative resistance *versus* strain curves of the four regions, and the GF values of the four regions are calculated separately. It was determined that the largest discrepancy in GF_1 was observed in regions 1 and 4, while the largest discrepancy in GF_2 was also noted in regions 1 and 4, the largest discrepancy in GF_3 was identified in regions 3 and 4, with a gap of 9.64%, 7.02%, and 11.67%, respectively. These error values are within acceptable limits, indicating excellent reproducibility of the eutectogels. The response of the strain sensors to varying strain rates was subsequently examined. As illustrated in Fig. 5(c), the sensors were capable of producing discernible and stable signals at both slow strain rates (10–20 mm min^{-1}) and fast strain rates (100–200 mm min^{-1}). In light of the fact that strain sensors will be subjected to repeated loading and unloading cycles in practical applications, we investigated the cyclic stability of strain sensors. To further investigate the stability of the strain sensor output signal, progressive cyclic tensile tests were conducted at both small (10–30%) and large (100–300%) strain levels (Fig. 5(d) and (e)). The findings demonstrate that the strain sensor is capable of maintaining uninterrupted and reliable signal output at both small and large strain levels, with a high resolution and signal-to-noise ratio. The response speed of the sensor was examined by loading 30% strain. As illustrated in Fig. S19 (ESI†), the response and recovery times of the strain sensors were 347 ms and 529 ms, respectively. As illustrated in Fig. 5(f), the strain sensor exhibits highly reproducible signals in 8000 consecutive loading–unloading cycles at 50% strain, further substantiating the exceptional cyclic stability of the strain sensor. Furthermore, the signals exhibited no significant drift during the constant strain, which suggests that the PAL66 eutectogel strain sensors are capable of responding to strains at faster rates and producing stable signals in practical application scenarios. The long-term stability of the strain sensor was also investigated. As illustrated in Fig. S20a and b (ESI†), the PAL66 strain sensor was extended to 200% in order to assess its sensitivity stability. The GF value for the 200% strain was approximately 2.75 on day 1 and 2.62 on day 7, exhibiting minimal variation. Secondly, the signal stability of the PAL66 strain transducer was examined on days 1, 3, 5, and 7. It was found that the waveform and amplitude of the sensed signals remained near stable values (Fig. S20c, ESI†). These findings suggest that the PAL66 strain sensor exhibits good long-term stability. In order to ascertain the effect of temperature on the sensing capability of the PAL66 strain sensor, the sensor's sensitivity was examined under continuous cooling conditions. Specifically, the sensor was stretched to 200%, and its GF was calculated in two segments (Fig. S21a–g, ESI†) and plotted as a function of temperature and GF value (Fig. S21h and i, ESI†). It was observed that the GF of the PAL66 strain sensors exhibited a decline with a reduction in temperature. Both GF_1 and GF_2 demonstrated a pronounced decrease at 0 °C and subsequently attained a stable value. By measuring its initial resistance at varying temperatures, it was determined that the initial resistance of PAL66 strain sensor increases with decreasing temperature (Fig. S22, ESI†). This phenomenon can be attributed to the fact that a decrease in temperature leads to a decrease in the ionic conduction rate inside the eutectogel, thereby increasing the initial resistance of the eutectogel and consequently decreasing GF. However, even when the temperature is lowered to −40 °C GF_1 and GF_2 are still able to remain at 1.13 and 2.33 respectively, which suggests that PAL66 sensors have the potential to be used in low temperature environments. Practical applications may encounter scenarios that alternate between ambient and low temperatures; therefore, the sensing performance of the PAL66 strain sensor at fluctuating temperatures was examined. As demonstrated in Fig. S23 (ESI†), when the temperature fluctuates between 25 °C and −30 °C, the relative resistance *versus* strain curves of the sensor maintains a consistent trend at a given temperature. Furthermore, when an external force is applied to the sensor, resulting in a strain of 200%, the peak signal stabilizes at approximately 340 at 25 °C and 274 at −30 °C. These results indicate that the PAL66 strain sensor is capable of operating properly at fluctuating temperatures. Finally, the adaptability of the APL66 strain sensor to dry environments was examined. From the preceding examination of the mass retention of PAL66 eutectogel in a dry environment (25 °C, 30% relative humidity), it can be observed that the mass of PAL66 eutectogel reaches equilibrium after 8 h. Consequently, the sensing performance of the PAL66 strain sensor was examined after they were placed in a dry environment for 12 h (Fig. S24, ESI†). It was observed that although the GF value decreased, the maximum GF remained at 1.88, and the PAL66 strain sensor continued to function adequately in the dry environment.

Applications of eutectogel-based strain sensor

The strain sensor based on PAL66 eutectogel exhibits excellent mechanical stability, anti-freezing properties, high sensing sensitivity, and cyclic stability, enabling its effective operation at low temperatures. As illustrated in Fig. 6(a), PAL66 strain sensors have been attached to the mechanical claw to monitor its motion. Strain sensors were affixed to a mechanical gripper to quantify the extent of bending when grasping objects of varying dimensions (Fig. 6(b)). The results demonstrate that the bending degree of the gripper can be monitored by a strain sensor in both room temperature (25 °C) and low temperature (−30 °C) environments, and the output signals are highly stable (Fig. 6(c) and Fig. S25, ESI†). Subsequently, strain sensors were attached to the robot's knees to monitor the degree of knee flexion during the act of walking (Fig. 6(d)). As illustrated in Fig. 6(e), the relative resistance change signals generated by the strain sensors exhibited precise correlation with the bending of the robot's knee during a 20-step walking cycle conducted at room temperature (25 °C) and low temperature (−30 °C). In addition to motion monitoring of robots, we also investigated the potential of PAL66 eutectogel-based strain sensors for use in the field of encrypted information transfer. As illustrated in Fig. 6(f), the spike signals and square models generated by the strain sensors with varying degrees of bending can be correlated with the dots and lines of the Morse code. This facilitates the generation of relevant information according to the principles governing the arrangement of dots and lines in Morse code. The strain sensor was utilized to output English words, including ''YES'', ''NO'', and ''DES'', at two distinct temperatures: 25 °C and −30 °C. Fig. 6(g)–(l) demonstrates that the output signals exhibit high readability, supporting the potential application of the PAL66 eutectogel strain sensor in encrypted information transmission.

Conclusion

In conclusion, the PAL eutectogel was fabricated *via* a one-step photopolymerization of AA and LMA in the presence of CTAB in a DES/H_2O binary solvent. The eutectogel with optimal overall performance was achieved by modifying the ratio of DES to water. The extensive hydrogen bonding network between DES and water molecules endowed the eutectogel with remarkable

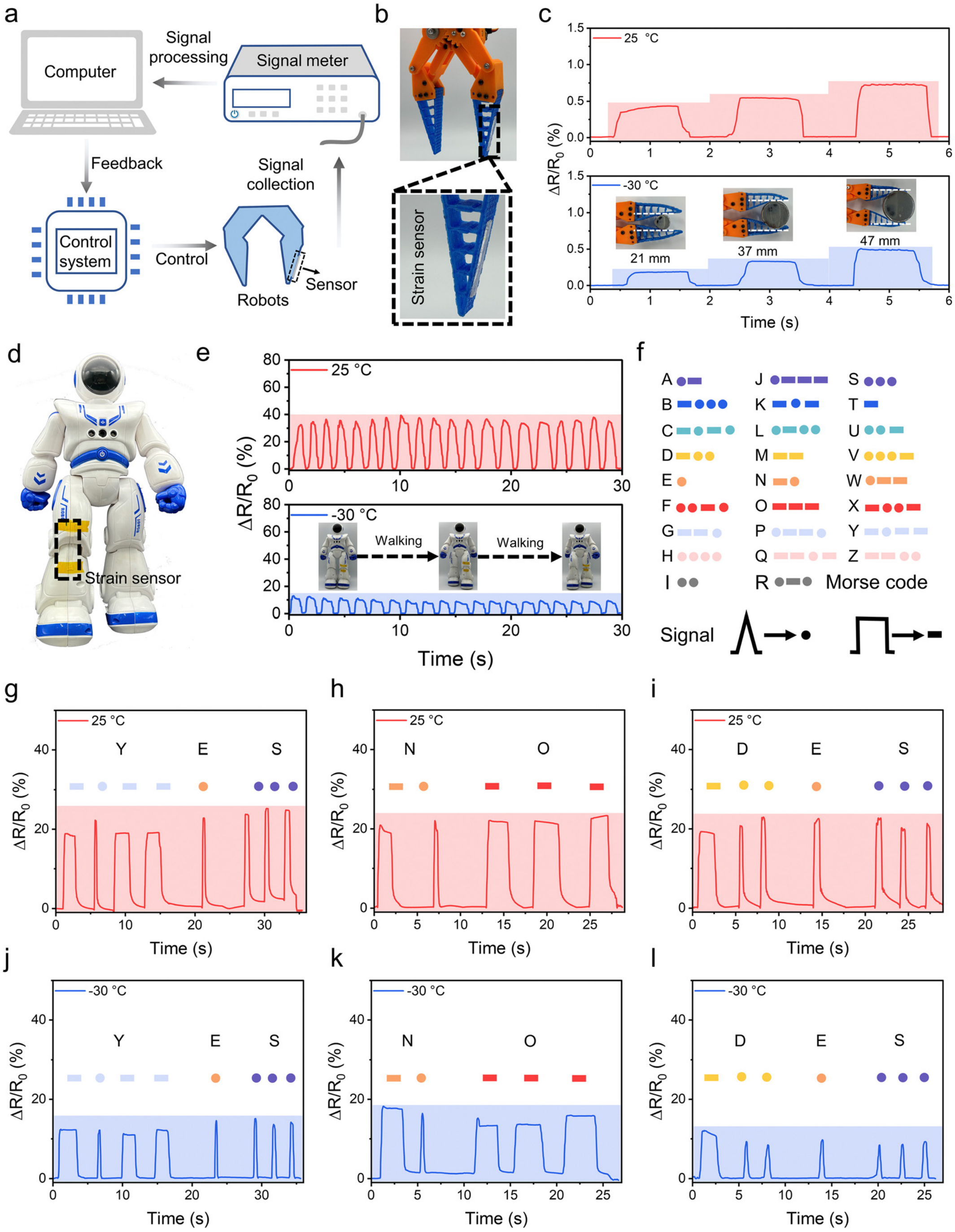

Fig. 6 Applications of PAL66 eutectogel-based strain sensors. (a) Schematic diagram of strain sensors monitoring robot motion. (b) and (c) Strain sensors monitor the degree of bending of robots gripping objects of different sizes. (d) and (e) Strain sensors monitor how much the robot's knees bend when walking. (f) Strain sensor output signal corresponds to Morse code. (g) Strain sensor output signal "YES" at 25 °C. (h) Strain sensor output signal "NO" at 25 °C. (i) Strain sensor output signal "DES" at 25 °C. (j) Strain sensor output signal "YES" at −30 °C. (k) Strain sensor output signal "NO" at −30 °C. (l) Strain sensor output signal "DES" at −30 °C.

environmental tolerance, reaching a freezing temperature of −60 °C. CTAB can establish stable hydrophobic binding sites with the polymer chain *via* hydrophobic interactions and electrostatic attraction. These areas function as dynamic physical cross-linking sites, endowing the eutectogel remarkable stretchability (elongation at break of 2890%) and anti-swelling properties (only 2% swelling in water over 7 days). Moreover, PAL66 eutectogel demonstrates commendable self-healing properties, achieving a self-healing efficiency of 59%. The polymer chain containing a significant quantity of –COOH and –COO$^-$ groups imparts advantageous adhesion characteristics to the eutectogel (14–25 kPa). Water can modulate the viscosity of the binary solvent, hence impacting the sensitivity of the eutectogel strain sensor. Consequently, we obtained highly sensitive eutectogel sensors (GF up to 15.4) by varying the DES/H_2O ratio. The eutectogel sensor was employed to track the motion of a robot and the transmission of an encrypted message at −30 °C, demonstrating remarkable adaptability in the low-temperature environment. This study provides significant insights that can guide the design and development of environmentally tolerant and high-sensitive eutectogel-based strain sensors.

Experimental section

Materials

Acrylic acid (AA, 99%) was purchased from Aladdin (China). Ethylene glycol (EG, 99%), choline chloride (ChCl, 99%), lauryl methacrylate (LMA, 99%), 2-hydroxy-4′-(2-hydroxyethoxy)-2-methylpropiophenone (Irgacure 2959, 98%), and cetyltrimethylammonium bromide (CTAB, 99%) were purchased from Adamas (China). All reagents were used directly without further purification.

Synthesis of DES

ChCl and EG were first mixed in a 1 : 2 molar ratio, and then the mixture was stirred at 90 °C for 2 h until it became a homogeneous and transparent solution.

Preparation of the PAL eutectogels

The precursor solutions were obtained by adding 1.5 g of AA, 0.15 g of LMA, 0.35 g of CTAB, and 8.25 mg of Irgacure 2959 to a binary solvent consisting of DES and water (the specific ratios of the binary solvents are detailed in Table S1, ESI†). Subsequently, the precursor solutions were introduced into a mold constructed using a glass plate and a silicone pad and left for 1 h under conditions that avoided the influence of light. Finally, the molds containing the precursor solution were irradiated under a 365 nm wavelength UV light (light intensity: 0.17 W cm^{-2}) for 0.5 h to obtain PAL eutectogels.

Characterization

ATR-FTIR spectra were measured by a Nicolet 5700 instrument (Nicolet Co., USA) with a resolution of 4 cm^{-1} over the range 500–4000 cm^{-1}. UV-Vis spectroscopy (Agilent Cary 60) was used to assess the transmittance of eutectogel samples with a length of 30 mm, a width of 10 mm and a thickness of 1 mm.

Mechanical measurements

The PAL eutectogel was cut into 30 × 5 × 1 mm^3 strips and tensile tests were carried out at a rate of 50 mm min^{-1}, each sample was tested at least 3 times. Continuous loading–unloading tests and cyclic loading–unloading tests are performed at the same rate. The dissipated energy is estimated based on the area between the loading–unloading curves, which is calculated by the following equation:

$$\text{Dissipated energy} = \int_0^{\varepsilon_f} \sigma_{\text{loading}} - \sigma_{\text{unloading}} \mathrm{d}\varepsilon \qquad (1)$$

where σ_{loading} and $\sigma_{\text{unloading}}$ refer to stress under loading and unloading processes, respectively. ε_f represents the strain at fracture.

For the compression test, the eutectogel needs to be prepared as a cylindrical sample with a height of 20 mm and a diameter of 10 mm. Both the compression test and the cyclic compression test were performed at a rate of 5 mm min^{-1}. All mechanical performances were evaluated by a universal testing machine (HZ-1004, Lixian Instrument Technology, China).

Environmentally tolerance performance of PAL eutectogel

The tolerance to desiccation, swelling in solvent, and freezing was studied. The eutectogels were cut into squares with 15 × 15 × 1 mm^3 and placed in a constant temperature and humidity incubator to examine the resistance to desiccation. The ambient conditions were set at 25 °C and 30% relative humidity. The mass retention rate was calculated by the following equation:

$$\text{Mass retention rate} = \frac{m}{m_0} \times 100\% \qquad (2)$$

where m_0 is the initial weight of the eutectogel and m is the weight of the eutectogel after a period of time in a constant temperature and humidity incubator.

The eutectogels were soaked in solutions with varying pH values of 3, 5, 7, 9, and 11 to examine the anti-swelling properties of the eutectogel. The swelling ratio was calculated by the following equation:

$$\text{Swelling ratio} = \frac{m - m_0}{m_0} \times 100\% \qquad (3)$$

where m_0 is the initial weight of the eutectogel and m is the weight of the eutectogel after a certain time of immersion.

The tolerance to freezing was then investigated. Eutectogels were stored in a cold trap at −60 °C for 2 h. The appearance of the eutectogels was observed, and the eutectogels were bent to determine if they had been frozen. The mechanical properties of PAL0 and PAL66 eutectogels were investigated under temperature varying conditions using a dynamic mechanical thermal analyzer (DMA, Q800, TA, USA). The stress–strain curves of PAL0 and PAL66 eutectogels were firstly tested at different temperatures (25, −30 and −60 °C). The energy storage modulus (G'), loss modulus (G'') and loss factor ($\tan\delta$) of PAL0 and PAL66 eutectogels were also tested by temperature scanning. The temperature range was −60 to 25 °C, the frequency was 1 Hz, and the amplitude was 15 μm. A differential scanning calorimeter (DSC, 2500, TA, USA) was used to characterize the anti-freezing properties of PAL eutectogels. The rate of heating/cooling was 1 °C min^{-1} and the temperature range was −80 °C to 25 °C.

Simulation methods

Molecular dynamics (MD) simulations were performed using the large-scale atomic/molecular massively parallel simulator

(LAMMPS) package (2 Aug 2023 – Update 3).[43,44] The model was built using Packmol and Moltemplate software.[45,46] The simulation box for the PAL66 eutectogel contained 8 P(AA-*co*-LMA) polymer chains (each comprising 40 repeating units), 16 CTAB molecules, 110 ChCl molecules, 220 EG molecules, and 800 water molecules, corresponding to the mass ratio of each component in the PAL66 eutectogel system. The SPC/E water model was used to simulate water molecules, and the SHAKE algorithm was applied to keep the water molecules rigid.[47,48] The OPLS-AA force field was used to describe all other molecules in the system.[49,50] MD simulations were performed using the NPT ensemble with a time step of 1 fs. The PAL66 eutectogel system was first subjected to energy minimization and then the system was slowly heated to 273 K (0 °C) within 1 ns. After that, the system was then relaxed at 273 K (0 °C) and 1 bar for 2 ns to reach equilibrium and finally the dynamics were run for 10 ns. The snapshots of the MD simulations were processed using the visual molecular dynamics (VMD) software.[51] The Python library MDAnalysis was used to analyze the hydrogen bonding of the PAL66 eutectogel system.[52]

Density functional theory (DFT) was applied to investigate the weak interactions between water molecules and DES in the system. All DFT calculations were performed using ORCA 5.0.4 package.[53] The specific computational procedure is as follows: firstly, geometry optimization and frequency calculations were performed using the B3LYP functional paired with the def2-TZVP basis set.[54–56] Dispersion corrections were applied using Grimme's D3 (BJ) method.[57,58] Subsequently, binding energies of water and DES were computed using the B3LYP functional and def2-TZVP basis set, with counterpoise (CP) corrections for basis set superposition error (BSSE).[59] The binding energy (ΔE_{int}) was calculated by the following equation:

$$\Delta E_{\text{int}} = E_{\text{AB}} - E_{\text{AB(A)}} - E_{\text{AB(B)}} \tag{4}$$

where E_{AB} represents the single-point energy of the composite system A and B. $E_{\text{AB(A)}}$ is the single-point energy of A which considers BSSE and $E_{\text{AB(B)}}$ is the single-point energy of B which considers BSSE. Weak interactions within the system were analyzed using the independent gradient model based on Hirshfeld partition (IGMH) method in Multiwfn 3.8 software, and the results were visualized using VMD software.[60,61]

Adhesion property of eutectogels

The lap-shear test was used to test the adhesion properties of eutectogel and different substrate materials, firstly eutectogel was cut into small pieces of 10 × 10 × 1 mm^3 and then pasted between two pieces of substrate and the samples were pulled at a fixed rate of 1 mm min^{-1} until the eutectogel and substrate separated, at least three samples of each eutectogel were prepared and used for testing. Adhesion strength was determined by dividing the maximum force by the overlap area. Adhesion strength in a high humidity environment was determined by placing the materials together in a constant temperature and humidity incubator (25 °C and 90% relative humidity) for 2 h after attaching them to the substrate before performing the lap shear test. The test procedure and the calculation of the adhesion strength are the same as those described above. A solution of pH = 3, 5, 7, 9, and 11 was added dropwise to the surface of the PAL66 eutectogel samples. The samples were left for 30 s and then affixed to a copper sheet. Adhesion strength was subsequently tested by lap-shear experiments. The test procedure and the calculation of the adhesion strength are the same as those described above.

Self-healing property of eutectogels

The eutectogel was cut into 30 × 10 × 1 mm^3 strips and then cut off at the center, ethanol was applied to the cut section and then the two cut sections were reassembled. The self-healing properties of the eutectogels were investigated by uniaxial tensile tests after being placed at 25 °C and −30 °C for 6 h, 12 h, and 24 h, respectively. The self-healing efficiency of the eutectogel was calculated from the breaking strength. The self-healing efficiency was calculated by the following equation:

$$\text{Self-healing efficiency} = \frac{\sigma}{\sigma_0} \times 100\% \tag{5}$$

where σ_0 is the breaking strength of the original eutectogels and σ is the breaking strength of the self-healed eutectogels.

Preparation and testing of strain sensor

The eutectogel was cut into strips of 30 × 10 × 1 mm^3 and two pieces of copper foil were applied to the ends of the eutectogel sample. A gauge factor (GF) was used to evaluate the sensitivity of the strain sensors. GF is defined as $(R - R_0)/(\varepsilon{\cdot}R_0)$, where R_0 is the initial resistance of the eutectogel when it is undeformed and R is the real-time resistance of the eutectogel when it is stretched to a given strain ε. All low-temperature performances of the eutectogel sensors were performed in a refrigerator. Sensing performance in dry environments is accomplished by incorporating a constant temperature and humidity incubator. A digital multimeter (DMM6500, Keithley, USA) and a universal testing machine (HZ-1004, Lixian Instrument Science and Technology, China) were used to apply strain to the strain sensors and record the resistance values.

Applications for monitoring motion and transmitting encrypted information

The Eutectogel was cut into 30 × 10 × 1 mm^3 strips and then attached to the outside of the grippers, and to the knees of the robot to monitor their motion. The same size of eutectogel was attached to the joints of the fingers, and two different signals were generated by bending and straightening the fingers, corresponding to the dots and dashes of the Morse code, for encrypted information transmission. During the experiments we controlled the ambient temperature to 25 °C and −30 °C.

Author contributions

Zhengen Wei: methodology, investigation, formal analysis, writing – original draft; Lianghao Jia: investigation, formal analysis, writing – original draft; Jinyu Yu: formal analysis, writing – original draft; Hanrui Xu: formal analysis, writing – original draft; Xing Guo: funding acquisition, writing – review & editing; Tao Xiang: conceptualization, supervision, funding acquisition, writing – review & editing; Shaobing Zhou: supervision, writing – review & editing.

Data availability

Data available on request from the authors.

Conflicts of interest

There are no conflicts to declare.

Acknowledgements

This work was supported by the National Natural Science Foundation of China (52103186, U22A20161 and 52033007), Sichuan Science and Technology Program (2024NSFTD0002) and the Fundamental Research Funds for the Central Universities (2682022JX001). The authors also thank the Analytical and Testing Center of Southwest Jiaotong University for providing the DSC measurements.

References

1 W. Guo and M. Ma, *J. Mater. Chem. A*, 2024, **12**, 9371–9399.
2 A. Roy, S. Zenker, S. Jain, R. Afshari, Y. Oz, Y. Zheng and N. Annabi, *Adv. Mater.*, 2024, **36**, 2404225.
3 L. Jia, J. Jiang, A. Ren, Z. Wei, T. Xiang and S. Zhou, *Chem. Eng. J.*, 2024, **495**, 153734.
4 L. Jia, Y. Li, A. Ren, T. Xiang and S. Zhou, *ACS Appl. Mater. Interfaces*, 2024, **16**, 32887–32905.
5 Y. Jian, S. Handschuh-Wang, J. Zhang, W. Lu, X. Zhou and T. Chen, *Mater. Horiz.*, 2021, **8**, 351–369.
6 M. Matsumoto, S. Saito and I. Ohmine, *Nature*, 2002, **416**, 409–413.
7 K. Lei, M. Chen, P. Guo, J. Fang, J. Zhang, X. Liu, W. Wang, Y. Li, Z. Hu, Y. Ma, H. Jiang, J. Cui and J. Li, *Adv. Funct. Mater.*, 2023, **33**, 2303511.
8 X. Huang, Z. Zheng, H. Wang, W. Xu, M. Wu, M. Wang, C. Chen, L. Wan, R. Du, T. Zhu, Z. Huang, X. Wang, X. Wang, Q. Zhang and X. Jia, *Adv. Funct. Mater.*, 2024, **34**, 2312149.
9 D. Jiang, H. Wang, S. Wu, X. Sun and J. Li, *Small Methods*, 2022, **6**, 2101043.
10 X. Yu, H. Zhang, Y. Wang, X. Fan, Z. Li, X. Zhang and T. Liu, *Adv. Funct. Mater.*, 2022, **32**, 2204366.
11 R. Liu, Y. Liu, S. Fu, Y. Cheng, K. Jin, J. Ma, Y. Wan and Y. Tian, *Small*, 2024, **20**, 2308092.
12 Y. Liu, L. Yin, S. Chen, Y. Liu, Q. Liu, L. Yang, Y. Li, Q. Zhang and Y. Huang, *J. Mater. Chem. A*, 2024, **12**, 18582–18592.
13 W. Shi, S. Jang, M. A. Kuss, O. A. Alimi, B. Liu, J. Palik, L. Tan, M. A. Krishnan, Y. Jin, C. Yu and B. Duan, *ACS Nano*, 2024, **18**, 7580–7595.
14 M. Gong, X. Wang, Z. Wu, L. Yue, Q. Chen, H. Li, X. Lin, L. Zhang and D. Wang, *Small*, 2024, **20**, 2400161.
15 H. Su, Q. Guo, C. Qiao, X. Ji, L. Gai and L. Liu, *Adv. Funct. Mater.*, 2024, **34**, 2316274.
16 B. B. Hansen, S. Spittle, B. Chen, D. Poe, Y. Zhang, J. M. Klein, A. Horton, L. Adhikari, T. Zelovich, B. W. Doherty, B. Gurkan, E. J. Maginn, A. Ragauskas, M. Dadmun, T. A. Zawodzinski, G. A. Baker, M. E. Tuckerman, R. F. Savinell and J. R. Sangoro, *Chem. Rev.*, 2021, **121**, 1232–1285.
17 H. Wu, Z. Pang, L. Ji, X. Pang, Y. Li and X. Yu, *Chem. Eng. J.*, 2024, **497**, 154883.
18 C. Wei, Y. Wang, Y. Liang, J. Wu, F. Li, Q. Luo, Y. Lu, C. Liu, R. Zhang, Z. Lu, B. Xu, N. Qing and L. Tang, *J. Mater. Chem. A*, 2024, **12**, 10392–10402.
19 Q. Cao and W. Yuan, *Chem. Eng. J.*, 2024, **494**, 153254.
20 J. A. Sirviö, R. Haataja, A. M. Kantola, T. Suopajärvi and H. Liimatainen, *Phys. Chem. Chem. Phys.*, 2022, **24**, 28609–28620.
21 A. Triolo, F. Lo Celso and O. Russina, *J. Mol. Liq.*, 2023, **372**, 121151.
22 Y. Zhao, H. Cheng, Y. Li, J. Rao, S. Yue, Q. Le, Q. Qian, Z. Liu and J. Ouyang, *J. Mater. Chem. A*, 2022, **10**, 4222–4229.
23 C. Fu, L. Shen, L. Liu, P. Tao, L. Zhu, Z. Zeng, T. Ren and G. Wang, *Adv. Mater.*, 2023, **35**, 2211237.
24 Z. Zhang, A. Yao and P. Raffa, *Adv. Funct. Mater.*, 2024, 2407529.
25 K. Fan, W. Wei, Z. Zhang, B. Liu, W. Feng, Y. Ma and X. Zhang, *Chem. Eng. J.*, 2022, **449**, 137878.
26 C. Chai, L. Ma, Y. Chu, W. Li, Y. Qian and J. Hao, *J. Colloid Interface Sci.*, 2023, **638**, 439–448.
27 Y. Song, L. Niu, P. Ma, X. Li, J. Feng and Z. Liu, *ACS Appl. Mater. Interfaces*, 2023, **15**, 10006–10017.
28 M. Li, Z. Liu, Y. Hu, R. A. Li and Y. Cao, *Chem. Eng. J.*, 2023, **472**, 145177.
29 Y. Pang, K. Zhang, X. Luan, B. Zhu, W. Shen, C. Xie, L. Li and J. Pang, *Chem. Eng. J.*, 2023, **477**, 146974.
30 D. Du, J. Zhou, T. Kaneko, W. Dong, M. Chen and D. Shi, *Chem. Eng. J.*, 2023, **474**, 145704.
31 O. E. Philippova, D. Hourdet, R. Audebert and A. R. Khokhlov, *Macromolecules*, 1996, **29**, 2822–2830.
32 U. Gulyuz and O. Okay, *Macromolecules*, 2014, **47**, 6889–6899.
33 C. Qi, Z. Dong, Y. Huang, J. Xu and C. Lei, *ACS Appl. Mater. Interfaces*, 2022, **14**, 30385–30397.
34 I. Pethes, I. Bakó and L. Pusztai, *Phys. Chem. Chem. Phys.*, 2020, **22**, 11038–11044.
35 S. Emamian, T. Lu, H. Kruse and H. Emamian, *J. Comput. Chem.*, 2019, **40**, 2868–2881.
36 Y. Liang, D. Zou, Y. Zhang and Z. Zhong, *Chem. Eng. J.*, 2023, **475**, 145928.
37 B. Guo, M. Yao, S. Chen, Q. Yu, L. Liang, C. Yu, M. Liu, H. Hao, H. Zhang, F. Yao and J. Li, *Adv. Funct. Mater.*, 2024, **34**, 2315656.
38 L. Fang, C. Zhang, W. Ge, M. Rong, F. Chen, Z. Chen, X. Wang, Z. Zheng and Q. Huang, *Chem. Eng. J.*, 2023, **478**, 147405.
39 L. Zhou, B. Zhao, J. Liang, F. Lu, W. Yang, J. Xu, J. Zheng, Y. Liu, R. Wang and Z. Liu, *Mater. Horiz.*, 2024, **11**, 3856–3866.

40 K. Xue, C. Shao, J. Yu, H. Zhang, B. Wang, W. Ren, Y. Cheng, Z. Jin, F. Zhang, Z. Wang and R. Sun, *Adv. Funct. Mater.*, 2023, **33**, 2305879.

41 Y. Liang, K. Wang, J. Li, H. Wang, X.-Q. Xie, Y. Cui, Y. Zhang, M. Wang and C.-S. Liu, *Adv. Funct. Mater.*, 2021, **31**, 2104963.

42 Q. Quan, C. Fan, N. Pan, M. Zhu, T. Zhang, Z. Wang, Y. Dong, Y. Wu, M. Tang, X. Zhou and M. Chen, *Adv. Funct. Mater.*, 2023, **33**, 2303381.

43 A. P. Thompson, H. M. Aktulga, R. Berger, D. S. Bolintineanu, W. M. Brown, P. S. Crozier, P. J. in't Veld, A. Kohlmeyer, S. G. Moore, T. D. Nguyen, R. Shan, M. J. Stevens, J. Tranchida, C. Trott and S. J. Plimpton, *Comput. Phys. Commun.*, 2022, **271**, 108171.

44 S. Plimpton, *J. Comput. Phys.*, 1995, **117**, 1–19.

45 L. Martínez, R. Andrade, E. G. Birgin and J. M. Martínez, *J. Comput. Chem.*, 2009, **30**, 2157–2164.

46 A. I. Jewett, D. Stelter, J. Lambert, S. M. Saladi, O. M. Roscioni, M. Ricci, L. Autin, M. Maritan, S. M. Bashusqeh, T. Keyes, R. T. Dame, J.-E. Shea, G. J. Jensen and D. S. Goodsell, *J. Mol. Biol.*, 2021, **433**, 166841.

47 H. J. C. Berendsen, J. R. Grigera and T. P. Straatsma, *J. Phys. Chem.*, 1987, **91**, 6269–6271.

48 V. Kräutler, W. F. van Gunsteren and P. H. Hünenberger, *J. Comput. Chem.*, 2001, **22**, 501–508.

49 G. A. Kaminski, R. A. Friesner, J. Tirado-Rives and W. L. Jorgensen, *J. Phys. Chem. B*, 2001, **105**, 6474–6487.

50 W. L. Jorgensen, D. S. Maxwell and J. Tirado-Rives, *J. Am. Chem. Soc.*, 1996, **118**, 11225–11236.

51 W. Humphrey, A. Dalke and K. Schulten, *J. Mol. Graphics*, 1996, **14**, 33–38.

52 N. Michaud-Agrawal, E. J. Denning, T. B. Woolf and O. Beckstein, *J. Comput. Chem.*, 2011, **32**, 2319–2327.

53 F. Neese, *Wiley Interdiscip. Rev.: Comput. Mol. Sci.*, 2022, **12**, e1606.

54 P. J. Stephens, F. J. Devlin, C. F. Chabalowski and M. J. Frisch, *J. Phys. Chem.*, 1994, **98**, 11623–11627.

55 F. Weigend and R. Ahlrichs, *Phys. Chem. Chem. Phys.*, 2005, **7**, 3297–3305.

56 A. Schäfer, C. Huber and R. Ahlrichs, *J. Chem. Phys.*, 1994, **100**, 5829–5835.

57 S. Grimme, S. Ehrlich and L. Goerigk, *J. Comput. Chem.*, 2011, **32**, 1456–1465.

58 S. Grimme, J. Antony, S. Ehrlich and H. Krieg, *J. Chem. Phys.*, 2010, **132**, 154104.

59 S.-i Kawahara, T. Uchimaru and K. Taira, *Chem. Phys.*, 2001, **273**, 207–216.

60 T. Lu and F. Chen, *J. Comput. Chem.*, 2012, **33**, 580–592.

61 T. Lu and Q. Chen, *J. Comput. Chem.*, 2022, **43**, 539–555.